PCCP

ROYAL SOCIETY OF CHEMISTRY

PAPER

View Article Online
View Journal | View Issue

Cite this: *Phys. Chem. Chem. Phys.*, 2025, **27**, 1366

Brightness and AIEE behaviour of methylenebis(4,1-phenylene) linkage electron donor–acceptor-based dyads and their implications for robust quantification of explosive picric acid in both aqueous medium and solid state†

Manas Mahato,[a] Tuhina Sultana,[a] Rajkumar Sahoo,[b] Sabbir Ahamed,[a] Najmin Tohora,[a] Arpita Maiti[a] and Sudhir Kumar Das *[a]

Received 10th November 2024,
Accepted 8th December 2024

DOI: 10.1039/d4cp04294h

rsc.li/pccp

Organic luminescent materials having photoluminescence in their solid state have become emerging trends in chemistry, materials science, and biology due to their versatile potential applications. In the present contribution, we have introduced some methylenebis(4,1-phenylene) electron donor–acceptor-based fashionable solid-state fluorescent molecules, **MBA**, **MBB**, and **MBH,** having exciting photoluminescence characteristics in their solid and aggregate states. Interestingly, all probes exhibited a compelling aggregation-induced enhanced emission (AIEE) phenomenon in aqueous media. The mechanistic aspects of solid-state brightness and AIEE behavior are elucidated by diverse spectroscopic, microscopic, and X-ray crystallographic analyses. Employing their intriguing AIEE characteristics, the water-suspended low dimensional particles have been employed as a sensor, demonstrating rapid sensitivity and brilliant selectivity towards the nitro-explosive compound picric acid (PA). The estimated limits of detection (LOD) and quantification (LOQ) reach as low as the μM to nM range in the aqueous medium. The fluorescent paper strip-based test kit experiment has been demonstrated for instant detection of PA through visual examination in the solid state, rendering the protocol quick, cost-effective, and appropriate for on-spot solid-state recognition.

1. Introduction

Many organic luminescent materials in chemistry, materials science, and biology have attracted a lot of attention because of their potential applications.[1–5] Several fluorogenic organic emitters are extremely emissive in their diluted solution, but when they are aggregated, their emissive property quickly vanishes.[6,7] This phenomenon is well-known as the aggregation caused quenching (ACQ) effect. However, many fluorescent substances are non-emissive in a good solvent but turn emissive when these are aggregated. This phenomenon is well known as the aggregation-induced emission (AIE) effect.[6,7] Another class of molecules exhibits aggregation-induced emission enhancement (AIEE), which is characterized by molecules that exhibit weak emission in a good solvent but strong emission when aggregated.[8–12] Their distinctive quality distinguishes them from traditional luminophores and drives research into how these photoluminescent materials might be useful in the design of optical sensors and other crucial optoelectronic applications. Fluorophores with AIEE features have been successfully employed in organic light-emitting diodes (OLEDs),[13,14] photoemitters,[15] electroluminescent materials,[16] and other devices as well as in sensors.[17–20] Their mechanisms are normally defined in terms of restricted intermolecular rotation (RIR),[21] intramolecular charge transfer (ICT),[22,23] excited-state proton transfer process,[24] and intramolecular hydrogen bonds,[25] among others. A lot of work has been carried out on developing synthetic organic nano/micro-particles with a range of sizes and shapes. This comprises zero-dimensional (0-D) tetrahedral or spherical quantum dots,[26] one-dimensional (1-D) nanorods and wires from small organic compounds,[27,28] two-dimensional (2-D) nanoplates,[29] and three-dimensional (3-D) cubic symmetry.[30] Many methods, including physical vapor deposition,[31] ultra-sonication,[32] microemulsion,[33]

[a] *Department of Chemistry, University of North Bengal, Raja Rammohunpur, Darjeeling, West Bengal, 734013, India. E-mail: sudhirkumardas@nbu.ac.in*
[b] *Department of Chemistry, Indian Institute of Technology, Kharagpur, West Bengal, 721302, India*

† Electronic supplementary information (ESI) available. See DOI: https://doi.org/10.1039/d4cp04294h

self-organization,[34–36] template method,[37] chemical reactions,[38–40] reprecipitation,[41] *etc.*, have been developed to prepare organic nano/microparticles. Among them, reprecipitation has come up as paramount to developing highly luminescent nanomaterials.

Again, solid-state brightness has become an emerging trend in the field of device engineering and applications of light-emitting devices (LEDs) with the goals of achieving high brightness and low-cost approaches.[13,42] Up to now, materials based on organic molecules have been maturely developed to apply for LED applications. However, to obtain organic LED (OLED) devices with high brightness, high efficiency, and low cost, there are still some techniques to be improved, especially in synthesizing molecules displaying high brightness in their solid state which is vital for device fabrication. The applications of LEDs in lighthouses have different requirements from those used in general illumination. The important new application from LEDs will broaden the new potential innovations required in enabling this technology to be suitable for implementation. The investigation of novel organic materials specifically for investigating the color rendering index is highly crucial to developing various coloring index OLEDs. In that sense, materials based on organic molecules are of paramount importance.

Recently, there has been a concerning surge in terrorist activity within remote locations, emphasizing the urgent necessity for swift identification of nitro-explosives commonly employed in the creation of lethal weapons[43,44] like grenades and bombs. Picric acid (PA) stands as a potent organic acid,[45] belonging to the family of polynitrated aromatic compounds renowned for their formidable explosive properties. Surpassing the potency of trinitrotoluene (TNT), its explosive characteristics made it a prevalent choice until the conclusion of World War I.[46] While PA is acknowledged in dye industries, pharmaceuticals, and chemical laboratories, its significance is overshadowed by pronounced health risks and having more explosive power in their solid state among all the explosive nitroaromatic compounds (NACs). Functioning as a potent irritant to the skin and eyes, it also poses a potential threat to organs within the respiratory system. It is essential to highlight that due to the high solubility of PA in water, there is a risk of contaminating soil and groundwater upon exposure. Consequently, the pursuit of robust sensors capable of detecting PA at extremely low concentrations is a compelling area of research,[47] crucial for averting both terrorist threats and environmental pollution. Numerous techniques have been utilized for nitroaromatic explosive detection.[48–50] Notably, fluorescence sensing enjoys widespread application due to its exceptional sensitivity, rapid response, straightforward sample preparation, and other advantageous features.[51–53] Despite the utilization of various π-electron-rich fluorescent organic polymers[54–56] and metal–organic architectures[57] to identify electron-deficient nitroaromatics, creating soluble and efficient organic chemosensors with high selectivity for PA remains an exceedingly challenging endeavor.[58–60] Duan and colleagues reported sensitive and selective detection of picric acid in aqueous media based on conjugated porous polymer nanoparticles.[61] He *et al.* developed a porous organic framework as a fluorescent chemosensor for the detection of 2,4,6-trinitrophenol in an environmental sample.[62] Yao *et al.* reported the selective detection of picric acid based on supramolecular self-assembly of a cationic perylene diamide in pure aqueous media.[63]

In our ongoing efforts to develop AIEE-active fluorescent sensors and solid-state brightness organic molecules, we have successfully prepared 1,1′-((1*E*,1′*E*)-((methylenebis(4,1-phenylene)) bis(azanylylidene)) bis(methanylylidene)) bis(naphthalene-2-ol) (**MBA**), 2,2′-((1*E*,1′*E*)-((methylenebis(4,1 phenylene)) bis(azanylylidene)) bis(methanylylidene))diphenol (**MBB**), and 4,4′-((1*E*,1′*E*)-((methylenebis(4,1-phenylene)) bis(azanylylidene)) bis(methanylylidene)) bis(5-(hydroxymethyl)-2-methylpyridin-3-ol) (**MBH**) through a straightforward condensation method in the current study (Scheme S1, ESI†). Among these, Singh and co-workers previously reported **MBB** as a fluorescent chemosensor for selectively sequential detection of aluminium (Al^{3+}) and perchlorate (ClO_4^-) ions.[64] Interestingly, **MBA**, **MBB**, and **MBH** display greenish and yellowish color photoluminescence under 365 nm UV lamp illumination in the solid state. Fascinatingly, the developed **MBA**, **MBB**, and **MBH** probes feature a ligand system that is highly versatile and extensively conjugated, incorporating a consciously added hydrophobic behavior into its backbone to impart a distinctly water-insoluble nature. This characteristic renders it suitable for generating robust fluorescent aggregates in aqueous mixtures. The detailed mechanistic features of solid-state brightness and AIEE behavior are revealed through diverse spectroscopic, microscopic, and X-ray crystallography analyses. Additionally, the robust yellowish and greenish light emitted by one-dimensional (1-D) rod-shaped low-dimensional particles endows the material with promising applications in explosive detection. At the same time, fluorescent paper-based test kits were fashioned for instant visual detection of PA in its solid phase, rendering the protocol swift, uncomplicated, and economically viable for on-spot identification.

2. Experimental section

2.1. Reagents and instruments

All the reagents required for **MBA**, **MBB** and **MBH** preparation are procured from Sigma-Aldrich and TCI Chemicals, India, and are utilized as received, without the need for additional purification steps. Dimethyl sulfoxide (DMSO) for analytical experiments is sourced from Merck, India. The nuclear magnetic resonance (NMR) spectra are recorded using a Bruker 400 MHz NMR instrument, with chemical shifts (δ) recorded in ppm, employing tetramethylsilane as an internal standard. Deuterated DMSO (DMSO-d_6) for NMR spectroscopy is acquired from Sigma-Aldrich, India. Fourier transform infrared (FT-IR) spectra are captured using a Bruker Optik GMBH FT-IR spectrometer. High-resolution mass spectrometry (HRMS) analysis is performed on an Agilent 6545XT AdvanceBio LC/Q-TOF spectrometer. The nitroaromatic compounds (NACs) utilized are procured from Sigma-Aldrich in India. Throughout the experiment, triple-distilled water is employed. UV-visible absorption spectra are recorded using a HITACHI U-2910, while photoluminescence spectral measurements under ambient

conditions are conducted with a HITACHI F-7100 using 5 nm excitation and emission slits, respectively, with a scan speed of 1200 nm min^{-1} using 400 V PMT voltage. Time-resolved lifetime decay profiles are recorded on an Edinburgh (Lifespec) time-correlated single-photon counting (TCSPC) system with an EPL diode laser of 375 nm wavelength. The signals are collected at a magic angle (54.7°) using a photomultiplier tube (H10720-01, Hamamatsu), and the instrument response function (IRF) of the TCSPC setup is ~179 ps. After deconvoluting the IRF, each decay curve is fitted utilizing the exponential decay function: $\tau(t) = \sum \alpha_i e^{-t/\tau_i}$ having χ^2 values near to unity where χ^2 denotes the goodness of fit parameter. The α_i and τ_i values are the experimentally obtained pre-exponential factors having corresponding lifetimes. Experimentally as-obtained pre-exponential factors are then normalized using the equations $a_i = \frac{\alpha_i}{\sum \alpha_i}$ to achieve actual pre-exponential factors. The average fluorescence lifetime is determined utilizing the equation: $\langle \tau \rangle = \frac{\sum a_i \tau_i}{\sum a_i}$.

2.2. Synthesis and characterizations

The synthesis process of our desired probes **MBA**, **MBB** and **MBH** is presented in Scheme 1 and Schemes S1–S3 (ESI†), and detailed procedures are presented in the experimental section of the ESI,† followed by one-step condensation of 4,4′-methylenediamine and three different reagents, 2-hydroxy-1-naphthaldehyde, 2-hydroxybenzaldehyde, and 3-hydroxy-5-(hydroxymethyl)-2-methylisonicotinaldehyde with acceptable yields of 92%, 94%, and 91%, respectively. The structures of our probes were fully characterized and analyzed using various conventional analytical techniques. The corresponding ^{1}H NMR, ^{13}C NMR, and infrared (IR) spectra, and high-resolution mass spectra (HRMS) (Fig. S1–S9, ESI†) are shown in the ESI.† Our probes **MBA**, **MBB** and **MBH** are insoluble in water but completely soluble in typical polar organic solvents, which makes it feasible to fabricate fluorescent organic micromaterials.

3. Results and discussion

3.1. Spectroscopic performance of neat probes

Solid amorphous probes **MBA**, **MBB** and **MBH** exhibit a robust emission band at 534 nm (Fig. 1a), 534 nm (Fig. S10a, ESI†), and 544 nm (Fig. S11a, ESI†), respectively, upon excitation using a 365 nm UV lamp. The wavelength of excitation is determined to be 372 nm, which corresponds to an emission wavelength of 545 nm. It is found that the emission and excitation spectra are nearly mirror images of one another. Stacks of aggregates can form when the moieties in **MBA**, **MBB**, and **MBH** interact with one another through intra-molecular hydrogen bonding and π–π interactions in the neat solid state. Under a 365 nm UV lamp, the neat probes **MBA** and **MBB** emit greenish (Fig. 1b and Fig. S10b, ESI†) and **MBH** emits yellow color (Fig. S11b, ESI†) with the corresponding CIE values (x = 0.2791, y = 0.6615) (Fig. 1c), (x = 0.2911, y = 0.6587) (Fig. S10c, ESI†), and (x = 0.3806, y = 0.5691) (Fig. S11c, ESI†), respectively. This observation led to the classification of neat probes as a photoluminescent ink. Its qualities as a security ink were then determined by examining its compatibility with various writing instruments and templates under semi-solid conditions. These days, photoluminescent ink pens are the most common writing instruments used for security purposes across the globe. To show off our tidy probes as a luminescent ink, we have aggregated our probes in a 90% water–DMSO mixture and the word SERB is written on several courier materials, including filter paper (Whatman-41) and a TLC plate, to verify their superiority. When exposed to 365 nm UV light from a portable lamp, the word glows brightly and exhibits greenish and yellowish photoluminescence similar to our well-organized tidy probes on the filter paper. It is also observed that the word's luminescence can be strongly influenced by the substrate's properties. Using straightforward micropipette tips, the aggregate ink will be combined on the surface of the TLC plate and Whatman-41 filter paper, the probes **MBA** and **MBB** emit a greenish color (Fig. 2 and Fig. S12, ESI†), and the probe **MBH** emits a yellowish color (Fig. S13, ESI†). It will not diffuse

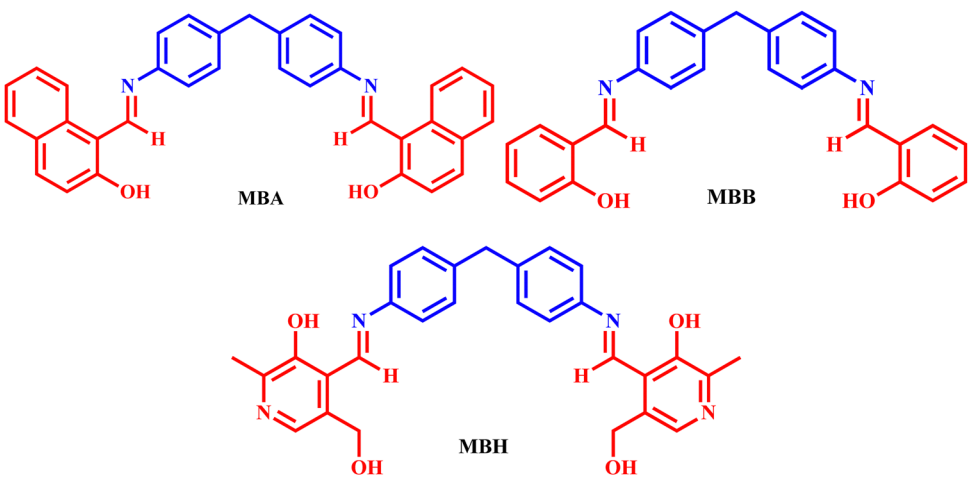

Scheme 1 Chemical structure of our desired probes **MBA**, **MBB** and **MBH**.

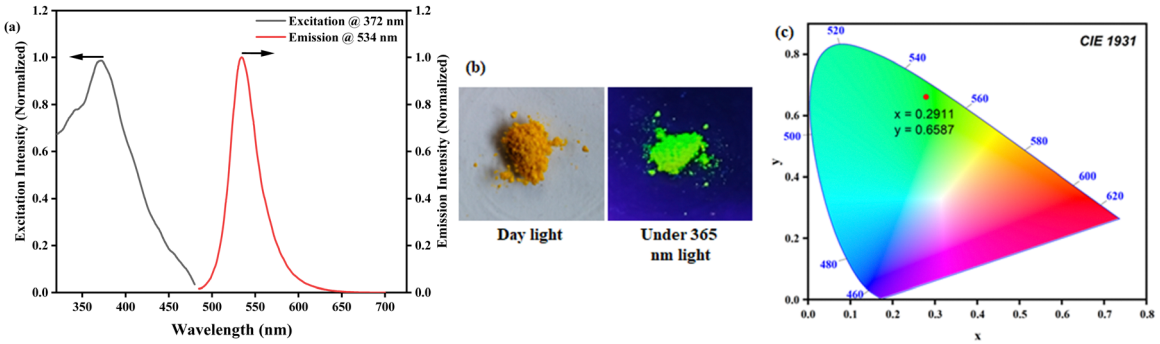

Fig. 1 (a) Excitation and emission spectra of our developed probe **MBA**, (b) photograph of our neat probe in daylight (left) and under 365 nm UV light (right), and (c) the corresponding color chromaticity diagram of our neat solid probe.

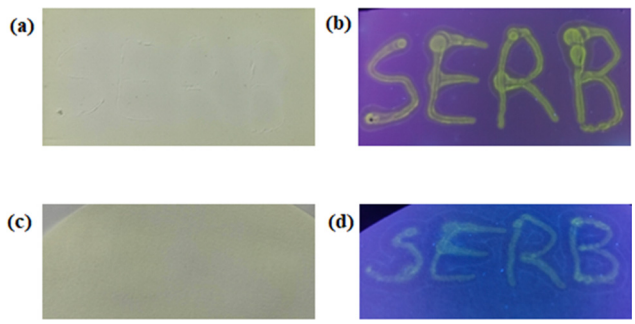

Fig. 2 Visibility of the word SERB, written using neat probe **MBB** in daylight (a) and (c) and under 365 nm UV light (b) and (d) on the surface of the TLC plate and Whatman-41 filter paper, respectively.

because it is difficult for the substrate to absorb. Conversely, a quiet halo is formed around the glowing word as the neat probes quickly soak up the filter paper (Whatman-41) (Fig. 2 and Fig. S12, S13, ESI†). That being said, the word's emissive quality is supposed to be pretty remarkable. Additionally, the neat amorphous probe ink displayed here can become an even more notable aid in the future when it is combined with these modern methods because aggregate particles are extremely compatible with several printing technologies, including fine print and 3D printing.

3.2. Synthesis of MBA, MBB, and MBH microparticles

The re-precipitation method was utilized to prepare the microstructure of probes **MBA**, **MBB**, and **MBH**. In a standard procedure, a small volume of 1 mM probes in DMSO was injected into 2 mL of unceasingly stirred 90% water–DMSO under ambient conditions for 30 min. The appearance of the water-suspended colloidal suspension verifies the formation of probe microparticles. To prepare microparticle solutions of different concentrations, different amounts of probe aliquots are introduced into 90% water–DMSO. Dynamic light scattering (DLS) and scanning electron microscopy (SEM) analysis confirm the formation of the microparticles. The hydrodynamic radius of water-suspended microparticles is determined to be within the nanometer range for **MBA** (350 nm ± 10 nm; Fig. 3a), **MBB** (500 nm ± 10 nm; Fig. S14a, ESI†), and **MBH** (600 nm ± 10 nm; Fig. S14b, ESI†). SEM image analysis indicates that the synthesized microparticles exhibit rod-shaped morphology with an average size of 400 nm, a finding corroborated by DLS analysis (Fig. 3b and Fig. S15, ESI†).

3.3. AIE behaviors of probes MBA, MBB, and MBH

The solid/aggregate state fluorescence emission characteristics of our probes **MBA**, **MBB**, and **MBH** were investigated using a conventional experiment with a good solvent–poor solvent. The probes are insoluble in water (a poor solvent), but are dissolved quickly in pure DMSO (a good solvent). It was found that the emission turned on the AIE character as the volume percentage of water in the mixed aqueous solution (DMSO/H_2O) increased gradually and the results are displayed in Fig. 4. When we slowly increased the percentage of water in DMSO/H_2O from 0% to 100%, the absorption spectra shifted to a higher wavelength (Fig. 4a and Fig. S16a, S17a, ESI†), which indicates the formation of J-aggregation. It is interesting to note that by slowly increasing the percentage of water in DMSO/H_2O from 60% to 90%, the photoluminescence intensity of the probes became noticeable and enhanced significantly. Upon excitation at 365 nm, two emission bands manifested: one featuring a sharp peak at 520 nm and the other exhibiting a broader band at 550 nm (Fig. 4b and Fig. S16b, S17b, ESI†). Under UV light illumination, the fluorescence was also enhanced in the mixed aqueous media due to aggregation, changing from its colorless solution to a sturdy fluorescent greenish and yellow color, as illustrated in Fig. 5 and Fig. S18 (ESI†). To better understand the emission behavior of the molecular form and aggregated state, a time-resolved fluorescence decay analysis of the probe and its aggregated states was carried out under excitation at 375 nm (Fig. 5b). The fluorescence decay profile of probe **MBB** in DMSO is found to be fitted with a tri-exponential function having τ_1 = 0.008 (97%), τ_2 = 2.577 (2%) and τ_3 = 4.333 (1%), respectively, with an average lifetime $\langle\tau\rangle$ = 0.105 ns. However, the fluorescence decay profiles of the **MBB** aggregate having a higher emission intensity at an excitation wavelength of 375 nm are fitted with bi-exponential functions τ_1 = 1.497 (24.2%), τ_2 = 3.169 (75.8%) with an average lifetime $\langle\tau\rangle$ = 2.765 ns, which confirms the AIEE behavior.

The reason behind the probe's distinct AIE nature was similar to the previously published articles.[65–67] The predominant

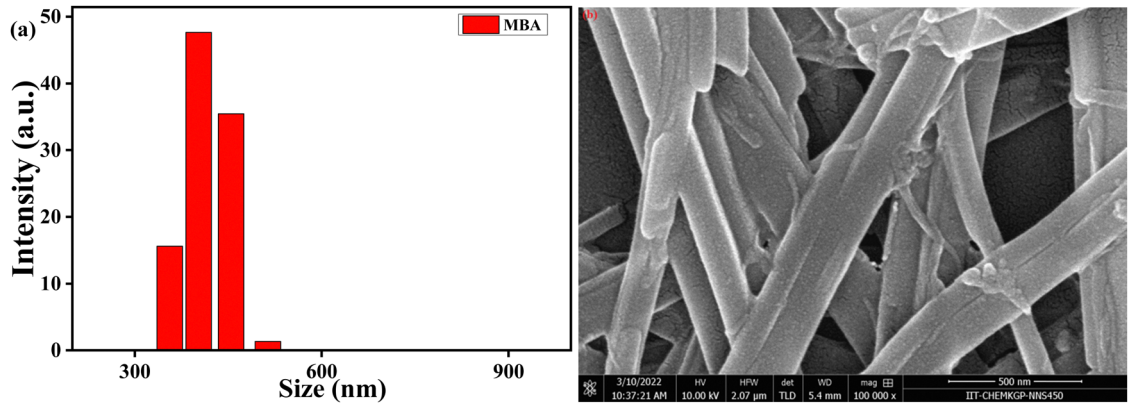

Fig. 3 (a) Dynamic light scattering (DLS) spectrum and (b) SEM images of the fabricated microparticles of our probe **MBA**.

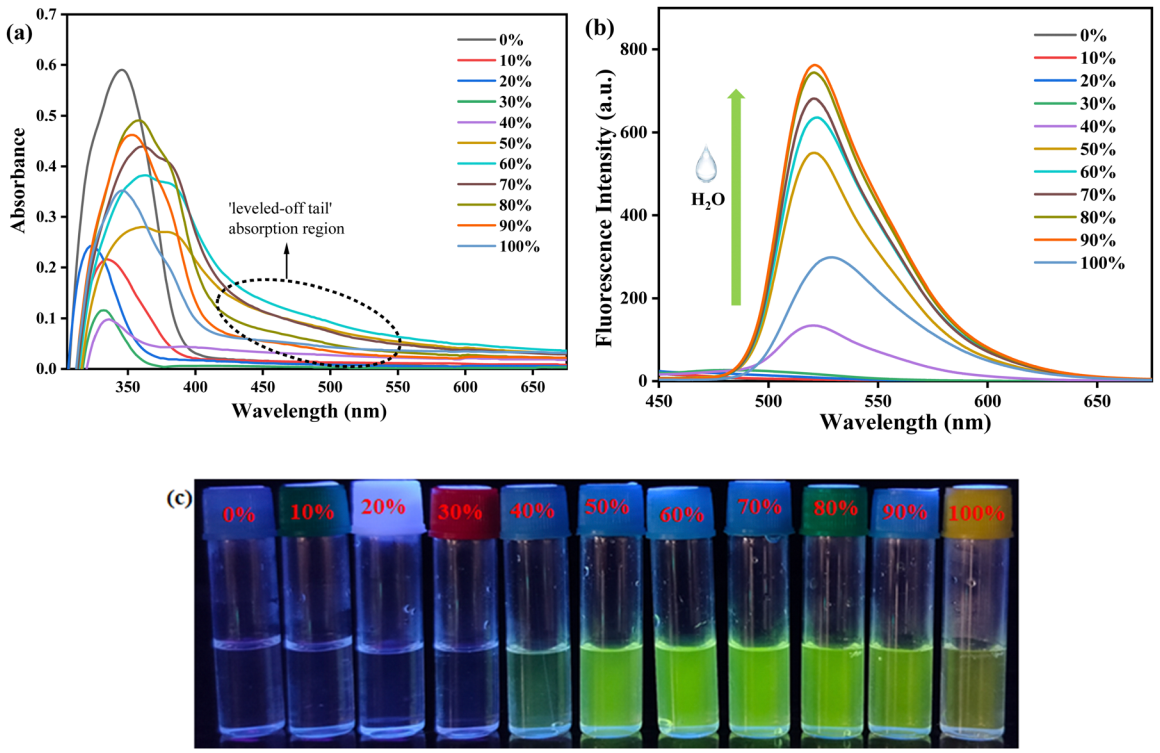

Fig. 4 (a) Changes in the absorbance spectrum of **MBB** upon increasing the water percentage in DMSO (from 0% to 100%). (b) Emission spectra of **MBB** in increasing aqueous medium (from 0% to 100%). (c) Pictorial representation of microparticle formation upon increasing the volume of water.

non-radiative decay in solution is primarily caused by unhindered intramolecular rotation.[68] Thus, one important factor contributing to the AIE features in aggregates is the restriction of intramolecular rotation (RIR).[69] The intramolecular rotation renders it non-emissive in the solution state due to efficient non-radiative decay. In contrast, aggregation in an H_2O/DMSO mixture with high water content effectively immobilized the intramolecular rotation through diverse intermolecular interactions. This locking mechanism sealed off the non-radiative pathway and opened up the radiative pathway, leading to a substantial enhancement in fluorescence intensity accompanied by a spectral redshift.[70] This was most likely caused by the intramolecular charge transfer (ICT) being suppressed and the probes achieving a reasonably planar geometry.

To examine the aggregation nature and various molecular interactions, we have utilized the cif file of 2,2′-(((methylenebis(azanylylidene))bis(methanylylidene)diphenol previously reported by Patra and co-workers. The crystallographic structure revealed the aggregation nature and the molecular interaction follows the same as they have reported previously.[71] Also the involvement of non-classical interactions was unveiled through the crystal engineering approach.[72] The involvement of non-covalent interactions is assessed by analyzing H-bonding interactions and C–H$\cdots\pi$ interactions. It is observed

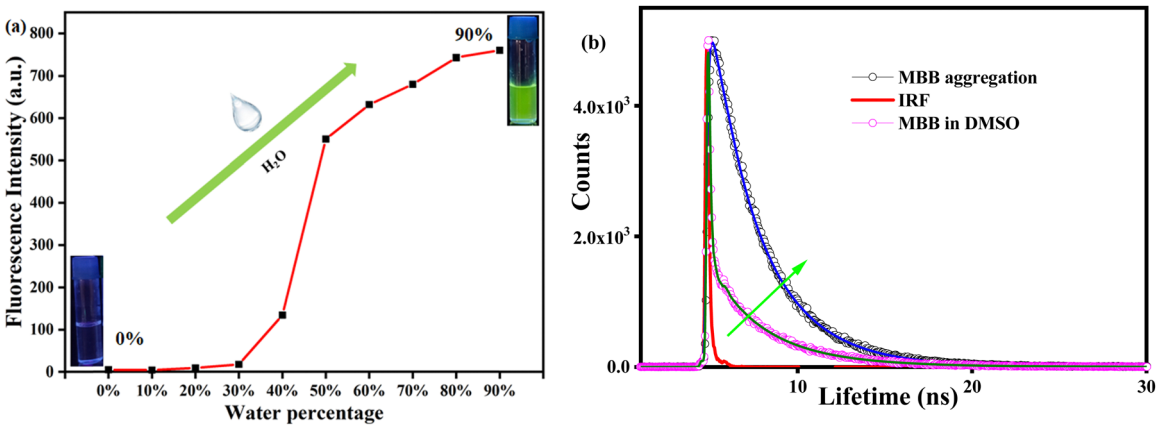

Fig. 5 (a) Emission intensity changes of probe **MBB** in the DMSO/H_2O mixture with different percentages of water. Inset: Pictorial representation of the change of 0% water (colorless) and 90% water (green color) under UV light (365 nm). (b) Time-resolved fluorescence decay curve of the probe **MBB** and **MBB** aggregates at $\lambda_{exc.}$ = 375 nm.

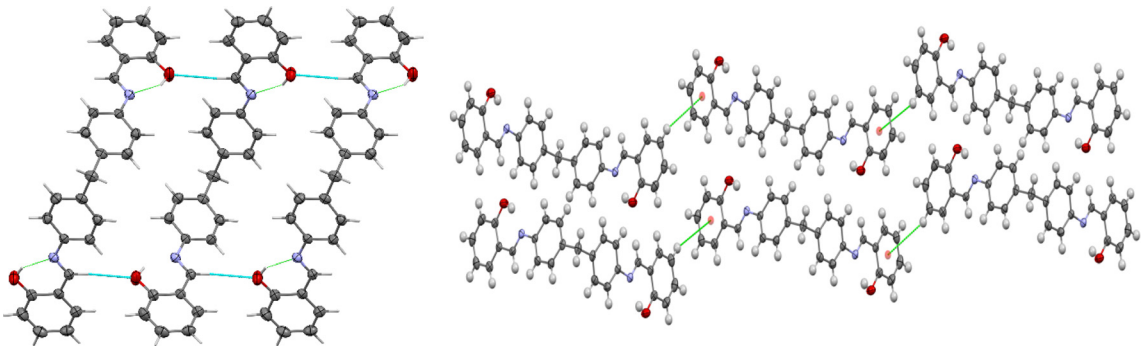

Fig. 6 (left) H-bonding interaction based supramolecular architecture; (right) C–H···π interaction mediated long-range framework in **MBB**.

that the proton of phenolic O–H makes an intramolecular H-bonding distance of 1.84 Å. In contrast, the phenolic-O forms a weak intermolecular H-bonding with the proton of azomethine-C with a distance of 2.54 Å. These intermolecular O···H interactions help to build a supramolecular architecture along the *ac* plane (Fig. 6). Furthermore, the molecule exhibited a 1D growth of the supramolecular framework through weak C–H···π interactions (3.46 Å) between the phenolic-CH and phenolic centroids, which is clear from the rod-shaped morphology of the water-suspended microaggregates.

Hirshfeld surface analysis was also carried out to understand the precise role of supramolecular interactions involved in the formation of the supramolecular framework. The Hirshfeld surface was generated by a 3D surface mapped over a fixed scale [**] [Fig. 7]. The shape index and curvedness were mapped ranging from −1.0 to 1.0 and −4.0 to 4.0, respectively. The red spot on the surfaces indicates the O···H interactions, while a relatively large green region is attributed to the presence of weak C–H···pi interactions in the compound. The 2D fingerprint plots were also extracted from the Hirshfeld analysis (Fig. 8). It is revealed that H···H, C···H, C···C, and O···H interactions are dominant in the crystal structure. Among these interactions, H···H intermolecular interactions are found to be most dominant as evidenced by their 53.3% contribution.

Yet, within this study, it has been noted that the absorption intensity diminishes as spectral redshift occurs, correlating with the rising volume percentage of water.[73–75] Conversely, the motional narrowing phenomenon gave rise to two novel bands at 415 nm and 490 nm.[76] Therefore, the UV-visible characteristics designate that substantial flexible compounds **MBB**, **MBA**, and **MBH** adopt an elongated planar geometry through an end-to-end parallel J-type arrangement (head-to-tail stacking) (Scheme 2) with their adjacent molecules in the solid/aggregated state.[73] The J-aggregate formation was confirmed through the discriminating emission spectrum of probes' aggregates, exhibiting spectral redshift in mixed aqueous media (H_2O/DMSO, 9 : 1, v/v), as opposed to the monomer's fluorescence emission observed in pure DMSO.[77] The emergence of the 'leveled-off tail' absorption in the 500–750 nm region (Fig. 4a and Fig. S16a, S17a, ESI†) resulted from the gradual increase in H_2O percentage, reaching up to 90%, induced by the scattering effect from preceding particles/aggregates in the aqueous solution.[77,78] These findings unequivocally suggest that the synthesized probes **MBB**, **MBA**, and **MBH** exhibit excellent AIE characteristics.

3.4. Detection ability to explosive picric acid (PA)

The developed **MBA**, **MBB** and **MBH** probes, initially non-fluorescent in pure DMSO, undergo a remarkable transformation

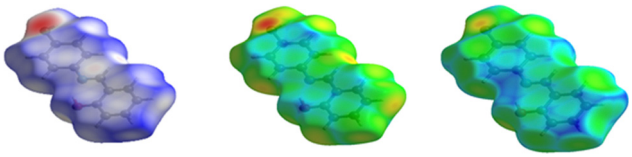

Fig. 7 Hirshfeld surfaces of **MBB**: left – 3D d_{norm} surface; middle – shape index; right – curvedness.

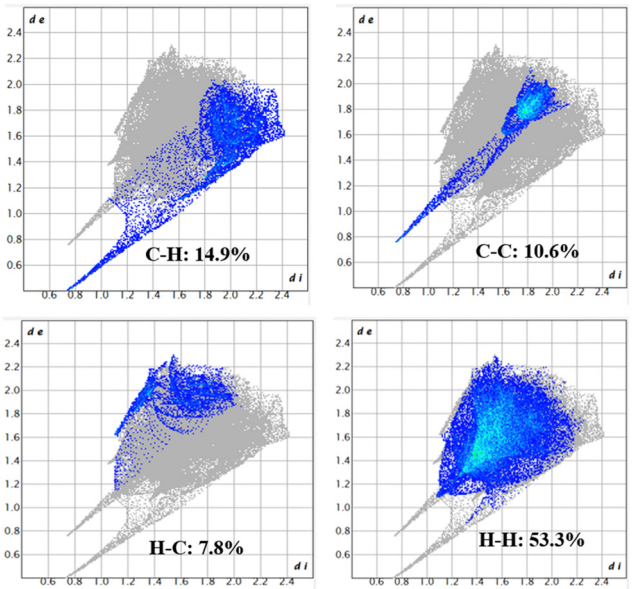

Fig. 8 2D fingerprint plots of the compound **MBB**.

into a highly emissive form when exposed to aqueous media with higher water percentages, leading to the formation of water-suspended microparticles with AIEE attractive properties. The intriguing AIE characteristics inspire us to utilize the intense greenish and yellow fluorescence of the fabricated microparticles as a sensor for detecting explosive NACs. Currently, there has been a rapid surge in terrorist activities within domestic locations, highlighting the urgent need for rapid detection of potentially explosive materials utilized in the design of lethal weapons. In the realm of nitroaromatics, PA exceeds TNT in explosive potency. Fortunately, our fabricated microparticles can identify small levels of PA in water with selectivity. We conducted emission titration studies in H_2O/DMSO (9 : 1, v/v) to examine its detection ability towards PA. This involved a quantifiable analysis of the interaction between the explosive PA and the fluorescent aggregates of the developed probes. As shown in Fig. 9 and Fig. S19 (ESI†), the photoluminescence titration was performed at room temperature. Interestingly, the pronounced photoluminescence intensity from aggregates at 520 nm (sharp band) and 545 nm (broadband) for **MBB** (Fig. 9), at 503 nm (sharp band) and 525 nm (broadband) for **MBA** (Fig. S19a, ESI†), and at 545 nm (sharp band) and 575 nm (broadband) for **MBH** (Fig. S19b, ESI†) underwent a gradual manifold reduction upon successive addition of PA (124 equiv., 90.3 equiv., and 85 equiv., respectively). Furthermore, the 'turn-off' fluorescence response is observed, revealing a noticeable fluorogenic color transition from bright green and yellow to a colorless solution upon the introduction of PA under a portable 365 nm UV lamp. This presents a promising opportunity for the naked-eye recognition of explosive PA employing a 365 nm UV lamp as a portable photonic device.

Moreover, the **MBA**, **MBB** and **MBH** microparticles serve as probes in fluorimetric analysis for the detection of NACs. To assess the selectivity and sensitivity of the fabricated microparticles for NAC detection, we introduced the same equivalents of various NACs, namely, picric acid (PA), 2-nitrophenol (2-NP), 4-nitrophenol (4-NP), 2,4-dinitrophenol (2,4-DNP), 2,4-dinitrotoluene (2,4-DNT), 4-nitroaniline (4-NA), nitrobenzene (NB) and 4-nitrobenzoic acid (4-NBA), into the water suspended microparticle solution, and subsequently recorded the photoluminescence spectra. PA exhibits pronounced emission quenching across all NACs, as illustrated in Fig. 10 and Fig. S20 (ESI†),

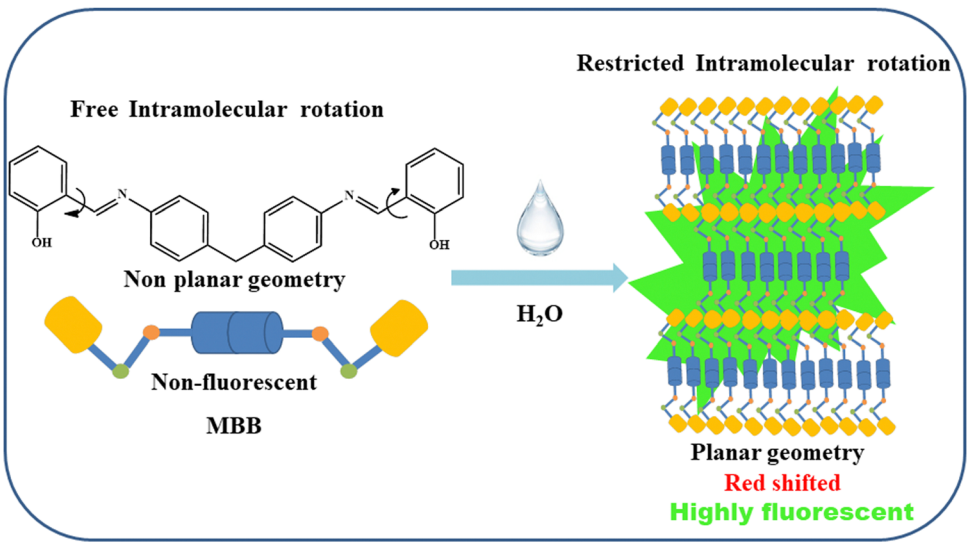

Scheme 2 Proposed molecular mechanism for **MBB**'s AIE behavior.

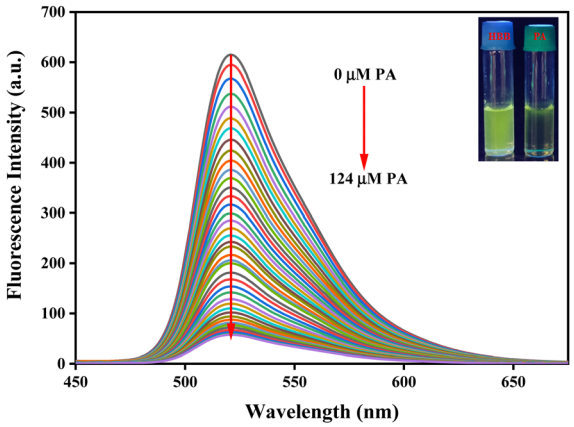

Fig. 9 Fluorescence titration spectra (λ_{ex} = 365 nm) of fluorescent **MBB** microparticles (comprising 99% water) while introducing various concentrations of PA. Inset: Visualization of the change from robust green color fluorescence to non-fluorescence in the presence of PA.

with the quenching characterized by both static and dynamic nature. The photoluminosity of the water-suspended microparticle solutions **MBA**, **MBB** and **MBH** at the emission wavelength 503, 520 and 545 nm, respectively, in the absence (I_0) and presence (I) of various NACs are nourished into the modified Stern–Volmer equation: $\frac{I_0}{I} = 1 + K_{SV}[Q]$, where K_{SV} and [Q] represent the quenching constant and concentration of the quencher, respectively. Fascinatingly, we found the nonlinear curve with an upward offset for PA (Fig. 11 and Fig. S21, ESI†). On the introduction of PA, the nonlinear Stern–Volmer behavior indicates that the fluorescence quenching of the microparticles is both static and dynamic. The static quenching could be related to the robust ground-state complexation between the fluorescent aggregates (electron-rich) and the foreign substance PA (electron-deficient) through a charge transfer mechanism, parallel to the previously reported articles,[79,80] and the dynamic quenching could be associated with the loss of planarity and disturbance in the aggregate behavior of the probe. We have estimated the quenching constant (K_{sv}) utilizing the linear Stern–Volmer equation plot (Fig. 11b) at a much lower concentration of quencher PA and obtained the values of 4.73×10^4 M^{-1}, 2.22×10^4 M^{-1} and 7.52×10^4 M^{-1} for **MBA**, **MBB** and **MBH**, respectively. Also, limits of detection (LOD) and quantification are determined by using the formulas LOD = 3σ/K and LOQ = 10σ/K, utilizing a linear calibration plot (Fig. 12 and Fig. S23, ESI†) acquired from a photoluminescence titration experiment and the obtained LODs are 5.97 nM for **MBB**, 0.39 μM for **MBA** and 89 nM for **MBH** and the LOQs are 20 nM for **MBB**, 1.3 μM for **MBA** and 0.3 μM **MBH**.

The quenching efficiency increases with increasing quencher concentration, which may be referred to as a super-magnified quenching effect, according to the plot of I_0/I *vs.* quencher concentration (Fig. 11a), which displays an upward curve rather than a linear relationship.[81–83] Here, the surface-bound **MBB** within the aggregated **MBB** serves as the active site for "turn-off" fluorescence in the presence of the quencher PA. This kind of quenching deviates from the Stern–Volmer plot as there is more than one of these active sites for a particular aggregated particle. The equation $\frac{I_0}{I} = 1.734e^{15\,900[PA]}$ is obtained by fitting the concave curve in Fig. 11a. The non-linear trend observed in the plot (Fig. 11a) indicates that both static and dynamic quenching of fluorescence intensity occur in the presence of the quencher PA. This ambiguity is clarified by measuring the fluorescence lifetime of the **MBB** aggregate in both the presence and absence of PA. The measured fluorescence decay curves of the **MBB** aggregate in both the presence and absence of PA are fitted with biexponential (Fig. 13 and Fig. S24, ESI†) decay having τ_1 = 1.497 (24.2%) and τ_2 = 3.169 (75.8%), and the fitted components are similar in both cases (Table 1). The fluorescence lifetime remains similar for **MBA**, **MBB**, and **MBH** in the absence and presence of PA, which suggests the nature of quenching is static, and it occurs from ground state complexation.

Detecting trace amounts of PA in the solid state is essential for assessing residual contamination and plays an important role in forensic and analytical sciences as it is highly explosive in the solid state among all the nitro-explosives.[84,85] In this context, we aimed to demonstrate solid-state screening investigations for

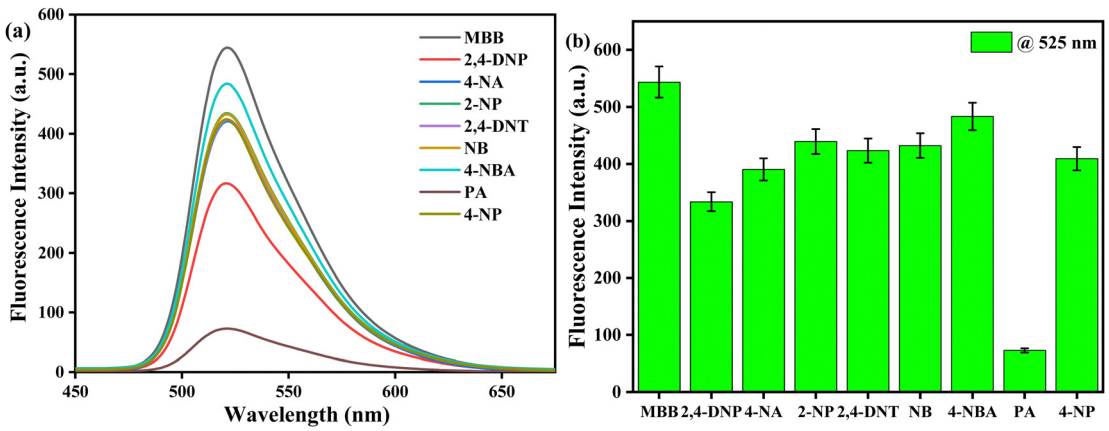

Fig. 10 (a) Emission spectra (λ_{ex} = 365 nm) of **MBB** microparticles with several NACs. (b) Bar plot of fluorescence quenching of **MBB** microparticles after the addition of various NACs.

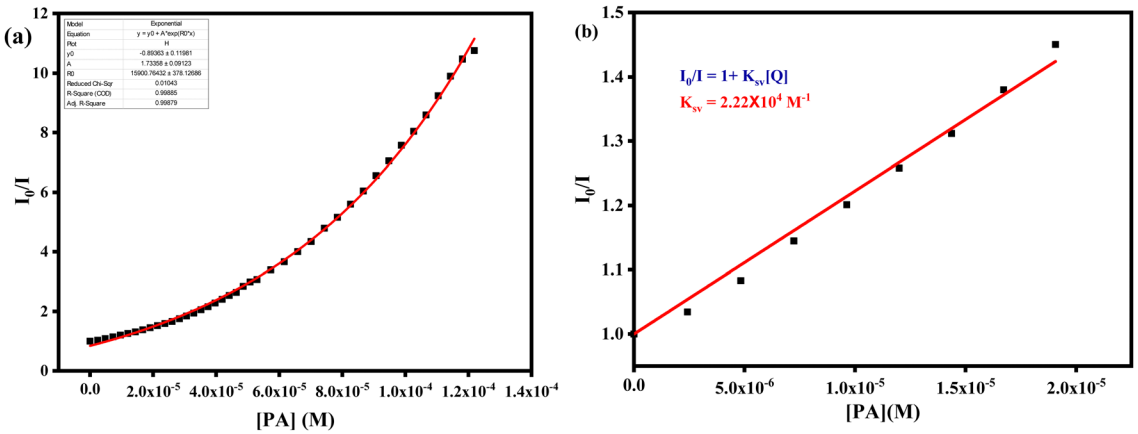

Fig. 11 (a) Stern–Volmer plot of the quenching of **MBB** microparticles on interaction with PA. (b) The linear Stern–Volmer curve of fluorescence quenching in the presence of a lower concentration of PA.

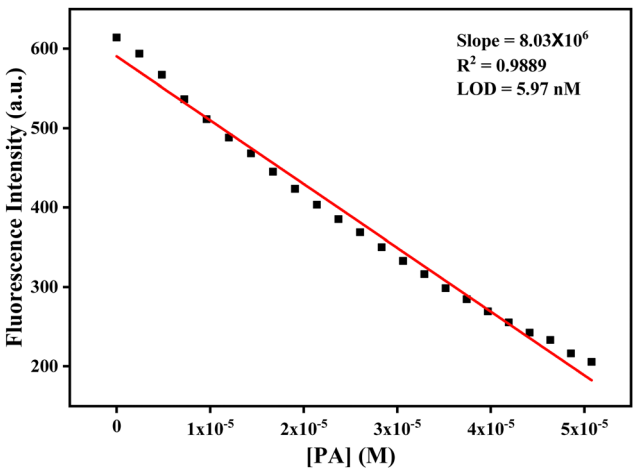

Fig. 12 The linear calibrations plot of [PA] *vs.* photoluminosity to estimate the LOD and LOQ values for the recognition of PA ions utilizing **MBB** microparticles.

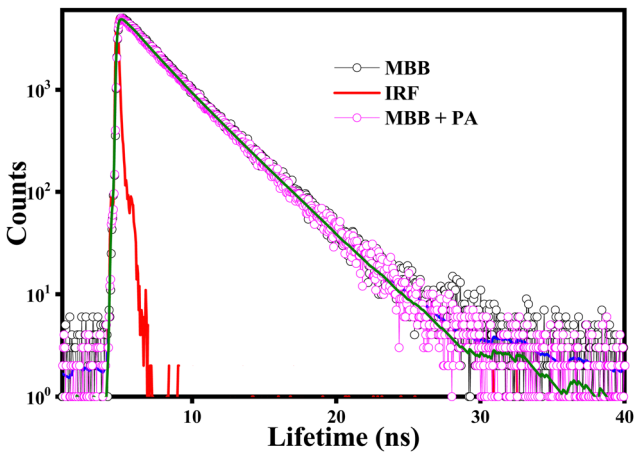

Fig. 13 Fluorescence lifetime decay profile of **MBB** microparticles in the absence and presence of PA.

visually distinguishing PA at the ppb level through selective 'turn-off' fluorescence responses. To achieve cost-effectiveness and portability, we have fabricated fluorescent test strips. After dip-coating Whatman filter papers with the probe aggregates, we proceeded to dry the test strips with the help of a hot air oven. The absorbing aggregates on the test strips exhibit intense green and yellow emissions with 'SKD' under 365 nm UV light illumination. These emissions turn non-fluorescent upon adsorbing the solution of PA, revealing a black mark labeled 'PA' within the previously intense green and yellow-colored fabricated test strips, as illustrated in Fig. 14A and Fig. S25, S26 (ESI†), respectively. For investigating the 'contact-mode' response, a solid crystal form of PA was applied to the test strips and subsequently detached after 10 seconds from the fluorescent paper strips. Black spots were detected in the contact zone under 365 nm UV light illumination, as displayed in Fig. 14B. Furthermore, to confirm the sensitivity in the solid state at various PA concentrations (10^{-3}–10^{-7} M), some TLC strips were made by adsorbing fluorescent probe aggregate solutions (Fig. 14C). These results point to another useful use of aggregates in the immediate "naked eye" detection of PA traces by "turn-off" fluorescence responses. This method has outstanding selectivity, sensitivity, speediness, and stability and does not require complex equipment or complicated operations.

Table 1 Time-resolved fluorescence lifetime decay parameters and average fluorescence lifetime of microparticles (**MBA**, **MBB**, and **MBH**) in the absence and presence of PA

	a_1[a]	τ_1[b] (ns)	a_2[a]	τ_2[b] (ns)	$\langle\tau\rangle$[c] (ns)	χ^2[d]
MBA	0.999	0.061	0.001	2.677	0.064	0.932
MBA + PA	0.998	0.06	0.002	2.67	0.066	1.21
MBB	0.242	1.497	0.758	3.169	2.765	1.16
MBB + PA	0.256	1.497	0.744	3.169	2.741	1.07
MBH	0.239	0.422	0.761	1.754	1.436	1
MBH + PA	0.254	0.422	0.746	1.754	1.416	1.04

[a] Pre-exponential factors. [b] Lifetimes in nanoseconds. [c] Average lifetimes in nanoseconds. [d] The goodness-of-fit parameters.

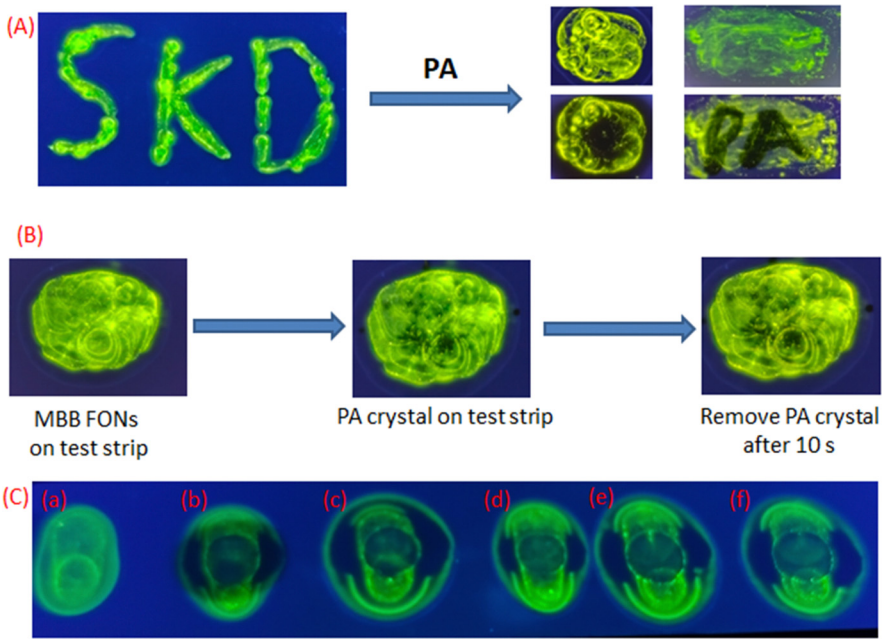

Fig. 14 (A) Pictorial representation of **MBB** water-suspended micromaterial absorbed test strip before and after the accumulation of PA. (B) Fluorescence image of the PA crystal on the test strip and after the removal of PA crystal after 10 s. (C) Fluorescence test strip image after introduction of various concentrations of PA: (a) **MBB** microparticles, (b) 10^{-3}, (c) 10^{-4}, (d) 10^{-5}, (e) 10^{-6}, and (f) 10^{-7}.

4. Conclusion

In summary, an investigation has been conducted into straightforward organic fluorescent sensors **MBA**, **MBB** and **MBH** that exhibit encouraging AIE phenomena with solid state brightness in both aqueous solution and amorphous states. Interestingly, they generate vivid green and yellow colored fluorescence in the amorphous state and water-suspended micro-aggregates in an aqueous medium, which have been demonstrated to be specific sensors for explosive PA in the μM to nM range. At the same time, fluorescent paper strips are employed to detect the amount of PA, allowing for an instantaneous "naked eye" response in a solid state and providing a quick and simple method for on-site visualization. To identify explosive PA in both solution and solid states, the current article presents a unique perspective on the design and development of solid-state photoluminescent molecules and fluorogenic sensors with attractive AIEE behavior.

Data availability

The data supporting this article have been included as part of the ESI.†

Conflicts of interest

There are no conflicts to declare.

Acknowledgements

Thanks to Anusandhan National Research Foundation (ANRF) erstwhile Science and Engineering Research Board (SERB), New Delhi, Govt. of India for the generous research grant (Grant No: EEQ/2023/00048). Thanks to the Govt. of West Bengal, India for providing the Swami Vivekananda Merit-cum-Means Scholarship to MM, TS, and SA. NT thanks the Ministry of Minority Affairs, Govt. of India for the Maulana Azad National Fellowship awarded to her. Heartfelt thanks to Prof. Mintu Halder, Indian Institute of Technology, Kharagpur for allowing us to record time-resolved fluorescence decay profiles in their TCSPC set-up. We are also indebted to Prof. B. Biswas of our department for helping us in the crystallographic discussion.

References

1 S. Lee, K. K. Y. Yuen, K. A. Jolliffe and J. Yoon, *Chem. Soc. Rev.*, 2015, **44**, 1749–1762.
2 H. N. Kim, Z. Guo, W. Zhu, J. Yoon and H. Tian, *Chem. Soc. Rev.*, 2010, **40**, 79–93.
3 D. W. Domaille, E. L. Que and C. J. Chang, *Nat. Chem. Biol.*, 2008, **4**, 168–175.
4 Z. Xu, J. Yoon and D. R. Spring, *Chem. Soc. Rev.*, 2010, **39**, 1996–2006.
5 P. Y. Gu, Z. Wang and Q. Zhang, *J. Mater. Chem. B*, 2016, **4**, 7060–7074.
6 S. W. Thomas, G. D. Joly and T. M. Swager, *Chem. Rev.*, 2007, **107**, 1339–1386.
7 Z. Ning, Z. Chen, Q. Zhang, Y. Yan, S. Qian, Y. Cao and H. Tian, *Adv. Funct. Mater.*, 2007, **17**, 3799–3807.
8 Z. Yang, W. Qin, N. L. C. Leung, M. Arseneault, J. W. Y. Lam, G. Liang, H. H. Y. Sung, I. D. Williams and B. Z. Tang, *J. Mater. Chem. C*, 2015, **4**, 99–107.

9 J. Mei, Y. Hong, J. W. Y. Lam, A. Qin, Y. Tang, B. Z. Tang, J. Mei, Y. Hong, J. W. Y. Lam, B. Z. Tang, A. Qin and Y. Tang, *Adv. Mater.*, 2014, **26**, 5429–5479.
10 P. Mazumdar, S. Maity, M. Shyamal, D. Das, G. P. Sahoo and A. Misra, *Phys. Chem. Chem. Phys.*, 2016, **18**, 7055–7067.
11 P. Mazumdar, D. Das, G. P. Sahoo, G. Salgado-Morán and A. Misra, *Phys. Chem. Chem. Phys.*, 2015, **17**, 3343–3354.
12 P. Mazumdar, D. Das, G. P. Sahoo, G. Salgado-Morán and A. Misra, *Phys. Chem. Chem. Phys.*, 2014, **16**, 6283–6293.
13 B. Yang, J. Xiao, J. I. Wong, J. Guo, Y. Wu, L. Ong, L. L. Lao, F. Boey, H. Zhang, H. Yang and Q. Zhang, *J. Phys. Chem. C*, 2011, **115**, 7924–7927.
14 G. Li, Y. Zhao, J. Li, J. Cao, J. Zhu, X. W. Sun and Q. Zhang, *J. Org. Chem.*, 2015, **80**, 196–203.
15 A. Hagfeldt and M. Grätzel, *Chem. Rev.*, 1995, **95**, 49–68.
16 G. Qian, B. Dai, M. Luo, D. Yu, J. Zhan, Z. Zhang, M. Dongge and Z. Y. Wang, *Chem. Mater.*, 2008, **20**, 6208–6216.
17 P. Mazumdar, S. Maity, D. Das, S. Samanta, M. Shyamal and A. Misra, *Sens. Actuators, B*, 2017, **238**, 1266–1276.
18 M. Shyamal, P. Mazumdar, S. Maity, G. P. Sahoo, G. Salgado-Morán and A. Misra, *J. Phys. Chem. A*, 2016, **120**, 210–220.
19 M. Shyamal, P. Mazumdar, S. Maity, S. Samanta, G. P. Sahoo and A. Misra, *ACS Sens.*, 2016, **1**, 739–747.
20 J. Li and Q. Zhang, *ACS Appl. Mater. Interfaces*, 2015, **7**, 28049–28062.
21 G. Yui, S. Yin, Y. Liu, J. Chen, X. Xu, X. Sun, D. Ma, X. Zhan, Q. Peng, Z. Shuai, B. Tang, D. Zhu, W. Fang and Y. Luo, *J. Am. Chem. Soc.*, 2005, **127**, 6335–6346.
22 J. Xu, X. Liu, J. Lv, M. Zhu, C. Huang, W. Zhou, X. Yin, H. Liu, Y. Li and J. Ye, *Langmuir*, 2008, **24**(8), 4231–4237.
23 X. Liang and Q. Zhang, *Sci. China Mater.*, 2017, **60**, 1093–1101.
24 T. He, X. T. Tao, J. X. Yang, D. Guo, H. B. Xia, J. Jia and M. H. Jiang, *Chem. Commun.*, 2011, **47**, 2907–2909.
25 K. A. N. Upamali, L. A. Estrada, P. K. De, X. Cai, J. A. Krause and D. C. Neckers, *Langmuir*, 2011, **27**, 1573–1580.
26 H. Yao and K. Ashiba, *RSC Adv.*, 2011, **1**, 834–838.
27 J. Xiao, H. Yang, Z. Yin, J. Guo, F. Boey, H. Zhang and Q. Zhang, *J. Mater. Chem.*, 2011, **21**, 1423–1427.
28 J. Xiao, B. Yang, J. I. Wong, Y. Liu, F. Wei, K. J. Tan, X. Teng, Y. Wu, L. Huang, C. Kloc, F. Boey, J. Ma, H. Zhang, H. Y. Yang and Q. Zhang, *Org. Lett.*, 2011, **13**, 3004–3007.
29 K. Ujiiye-Ishii, E. Kwon, H. Kasai, H. Nakanishi and H. Oikawa, *Cryst. Growth Des.*, 2008, **8**, 369–371.
30 Z. Q. Lin, P. J. Sun, Y. Y. Tay, J. Liang, Y. Liu, N. E. Shi, L. H. Xie, M. D. Yi, Y. Qian, Q. L. Fan, H. Zhang, H. H. Hng, J. Ma, Q. Zhang and W. Huang, *ACS Nano*, 2012, **6**, 5309–5319.
31 P. Salazar, V. Rico and A. R. González-Elipe, *Sens. Actuators, B*, 2016, **226**, 436–443.
32 Y. S. Zhao, W. Yang and J. Yao, *Phys. Chem. Chem. Phys.*, 2006, **8**, 3300–3303.
33 P. Verma and H. Pal, *J. Phys. Chem. A*, 2013, **117**, 12409–12418.
34 M. Jaseer and E. Prasad, *J. Photochem. Photobiol., A*, 2010, **214**, 248–256.
35 J. Li, P. Li, J. Wu, J. Gao, W. W. Xiong, G. Zhang, Y. Zhao and Q. Zhang, *J. Org. Chem.*, 2014, **79**, 4438–4445.
36 J. Li and Q. Zhang, *Synlett*, 2013, 686–696.
37 S. P. Anthony and S. M. Draper, *J. Phys. Chem. C*, 2010, **114**, 11708–11716.
38 J. Xiao, Z. Yin, H. Li, Q. Zheng, F. Boey, H. Zhang and Q. Zhang, *J. Am. Chem. Soc.*, 2010, **132**, 6926–6928.
39 Y. Liu, F. Boey, Luciana L. Lao, H. Zhang, X. Liu, Q. Zhang, Y. Liu, F. Boey, L. L. Lao, H. Zhang, Q. Zhang and X. Liu, *Chem. – Asian J.*, 2011, **6**, 1004–1006.
40 J. Xiao, D. Y. Kusuma, Y. Wu, F. Boey, H. Zhang, P. S. Lee and Q. Zhang, *Chem. – Asian J.*, 2011, **6**, 801–803.
41 S. Maity, P. Mazumdar, M. Shyamal, G. P. Sahoo and A. Misra, *Spectrochim. Acta, Part A*, 2016, **157**, 61–68.
42 L. Kacenauskaite, S. G. Stenspil, A. H. Olsson, A. H. Flood and B. W. Laursen, *J. Am. Chem. Soc.*, 2022, **144**, 19981–19989.
43 J. F. Xiong, J. X. Li, G. Z. Mo, J. P. Huo, J. Y. Liu, X. Y. Chen and Z. Y. Wang, *J. Org. Chem.*, 2014, **79**, 11619–11630.
44 V. Bhalla, A. Gupta and M. Kumar, *Org. Lett.*, 2012, **14**, 3112–3115.
45 G. V. Perez and A. L. Perez, *J. Chem. Educ.*, 2000, **77**, 910–915.
46 H. Muthurajan, R. Sivabalan, M. B. Talawar and S. N. Asthana, *J. Hazard. Mater.*, 2004, **112**, 17–33.
47 M. Nipper, Y. Qian, R. S. Carr and K. Miller, *Chemosphere*, 2004, **56**, 519–530.
48 D. S. Moore, *Rev. Sci. Instrum.*, 2004, **75**, 2499–2512.
49 Y. Zimmermann and J. A. C. Broekaert, *Anal. Bioanal. Chem.*, 2005, **383**, 998–1002.
50 L. J. Soltzberg, A. Hagar, S. Kridaratikorn, A. Mattson and R. Newman, *J. Am. Soc. Mass Spectrom.*, 2007, **18**, 2001–2006.
51 M. E. Germain and M. J. Knapp, *Chem. Soc. Rev.*, 2009, **38**, 2543–2555.
52 S. Shanmugaraju, S. A. Joshi and P. S. Mukherjee, *J. Mater. Chem.*, 2011, **21**, 9130–9138.
53 Y. H. Lee, H. Liu, J. Y. Lee, S. H. Kim, S. K. Kim, J. L. Sessler, Y. Kim and J. S. Kim, *Chem. – Eur. J.*, 2010, **16**, 5895–5901.
54 S. J. Toal and W. C. Trogler, *J. Mater. Chem.*, 2006, **16**, 2871–2883.
55 S. W. Thomas, G. D. Joly and T. M. Swager, *Chem. Rev.*, 2007, **107**, 1339–1386.
56 K. K. Kartha, S. S. Babu, S. Srinivasan and A. Ajayaghosh, *J. Am. Chem. Soc.*, 2012, **134**, 4834–4841.
57 V. Vajpayee, H. Kim, A. Mishra, P. S. Mukherjee, P. J. Stang, M. H. Lee, H. K. Kim and K. W. Chi, *Dalton Trans.*, 2011, **40**, 3112–3115.
58 Y. Peng, A. J. Zhang, M. Dong and Y. W. Wang, *Chem. Commun.*, 2011, **47**, 4505–4507.
59 G. He, H. Peng, T. Liu, M. Yang, Y. Zhang and Y. Fang, *J. Mater. Chem.*, 2009, **19**, 7347–7353.
60 B. Gole, S. Shanmugaraju, A. K. Bar and P. S. Mukherjee, *Chem. Commun.*, 2011, **47**, 10046–10048.
61 W. Zhang, Q. Cui, X. Guo, T. Ouyang, W. Dong and Q. Duan, *Microchem. J.*, 2022, **183**, 108022.
62 T. Huo, B. Yang and Y. He, *Microchem. J.*, 2024, **205**, 111271.
63 W. Zheng, Y. Zhao, X. Lin, Q. Zhang, K. Xiao, N. Cheng, X. Mei, Y. Lu and Z. Yao, *Dyes Pigm.*, 2022, **207**, 110761.

64 K. Kaur, V. K. Bhardwaj, N. Kaur and N. Singh, *Inorg. Chem. Commun.*, 2012, **26**, 31–36.
65 M. Shyamal, P. Mazumdar, S. Maity, S. Samanta, G. P. Sahoo and A. Misra, *ACS Sens.*, 2016, **1**, 739–747.
66 M. Shyamal, P. Mazumdar, S. Maity, G. P. Sahoo, G. Salgado-Morán and A. Misra, *J. Phys. Chem. A*, 2016, **120**, 210–220.
67 M. Shyamal, S. Maity, A. Maity, R. Maity, S. Roy and A. Misra, *Sens. Actuators, B*, 2018, **263**, 347–359.
68 J. Chen, C. C. W. Law, J. W. Y. Lam, Y. Dong, S. M. F. Lo, I. D. Williams, D. Zhu and B. Z. Tang, *Chem. Mater.*, 2003, **15**, 1535–1546.
69 Y. Huang, Z. Wang, Z. Chen and Q. Zhang, *Angew. Chem., Int. Ed.*, 2019, **58**, 9696–9711.
70 R. Hu, E. Lager, A. Aguilar-Aguilar, J. Liu, J. W. Y. Lam, H. H. Y. Sung, I. D. Williams, Y. Zhong, K. S. Wong, E. Peña-Cabrera and B. Z. Tang, *J. Phys. Chem. C*, 2009, **113**, 15845–15853.
71 G. K. Patra and D. De, *Eur. J. Chem.*, 2022, **13**, 49–55.
72 S. Kundu, S. Saha, A. Das, L. Singla, A. Roy Choudhury and B. Biswas, *J. Mol. Liq.*, 2022, **347**, 118340.
73 W. I. Gruszecki, *J. Biol. Phys.*, 1991, **18**, 99–109.
74 Z. Huang, X. Zhang, X. Zhang, B. Yang, Y. Zhang, K. Wang, J. Yuan, L. Tao and Y. Wei, *Polym. Chem.*, 2015, **6**, 2133–2138.
75 H. Ye, G. Liu, S. Liu, D. Casanova, X. Ye, X. Tao, Q. Zhang and Q. Xiong, *Angew. Chem., Int. Ed.*, 2018, **57**, 1928–1932.
76 A. Eisfeld and J. S. Briggs, *Chem. Phys.*, 2002, **281**, 61–70.
77 H. Ma, M. Yang, C. Zhang, Y. Ma, Y. Qin, Z. Lei, L. Chang, L. Lei, T. Wang and Y. Yang, *J. Mater. Chem. B*, 2017, **5**, 8525–8531.
78 Z. Huang, Q. Chen, Q. Wan, K. Wang, J. Yuan, X. Zhang, L. Tao and Y. Wei, *Polym. Chem.*, 2017, **8**, 4805–4810.
79 S. S. Pasha, H. R. Yadav, A. R. Choudhury and I. R. Laskar, *J. Mater. Chem. C*, 2017, **5**, 9651–9658.
80 V. Kachwal, P. Alam, H. R. Yadav, S. S. Pasha, A. Roy Choudhury and I. R. Laskar, *New J. Chem.*, 2018, **42**, 1133–1140.
81 S. Maity, M. Shyamal, P. Mazumdar, G. P. Sahoo, R. Maity, G. Salgado-Morán and A. Misra, *J. Mol. Liq.*, 2016, **224**, 255–264.
82 X. Sun, Y. Wang and Y. Lei, *Chem. Soc. Rev.*, 2015, **44**, 8019–8061.
83 J. Wang, J. Mei, W. Yuan, P. Lu, A. Qin, J. Sun, Y. Ma and B. Z. Tang, *J. Mater. Chem.*, 2011, **21**, 4056–4059.
84 A. H. Harris, O. F. Binkley and B. M. Chenoweth, *Am. J. Public Health Nation's Health*, 1946, **36**, 727–733.
85 J. F. Wyman, M. P. Serve, D. W. Hobson, L. H. Lee and D. "E" Uddin, *J. Toxicol. Environ. Health, Part A*, 1992, **37**, 313–327.